Computers and Structures 281 (2023) 107032

Contents lists available at ScienceDirect

Computers and Structures

journal homepage: www.elsevier.com/locate/compstruc

Short-horizon acceleration-predictive control for reducing lateral seismic inertia forces of inelastic frame structures using semi-active fluid viscous dampers

Assaf Shmerling [a,*], Matthias Gerdts [b]

[a] Department of Civil and Environmental Engineering, Ben-Gurion University of the Negev, Beer-Sheva 84105, Israel
[b] Institute of Applied Mathematics and Scientific Computing, Universität der Bundeswehr München, Neu-biberg, 85577, Germany

ARTICLE INFO

Article history:
Received 17 November 2022
Accepted 18 March 2023
Available online 30 March 2023

Keywords:
Semi-active fluid viscous damper
Short-horizon predictive control
Kalman filter
Inelastic frame structures
Earthquake response

ABSTRACT

Semi-active control systems effectively improve the resilience of civil structures when subject to dynamic vibrations due to their ability to change their damping properties. In the case of semi-active fluid viscous dampers (SAFVD), the damping coefficient quantity varies according to the tradeoff between the need to increase the energy dissipation capabilities (i.e., increasing the damping coefficient) and the need to decrease the applied shear forces (i.e., reducing the damping coefficient). The operation of a SAFVD device is similar to that of a passive fluid viscous damper except that, based on the status of the control valve, it can deliver damping at two distinct levels (two-stage) or over a wide range between an upper and lower bound (continuously adjustable). This paper employs a continuously adjustable SAFVD assembly and develops its optimal command voltage change at each time step, which regulates the valve that determines the fluid passing through the external path. The control strategy uses total acceleration measurement as the system's closed-loop feedback and utilizes the Kalman filter model to predict the sequential acceleration reading to cater to time delays. The solution derives from a short-horizon problem whose objective is reducing the difference between the lateral seismic inertia forces and the SAFVD forces, thus, mitigating the columns' resisting forces. The case study presented in this paper showcases the effectiveness of the SAFVDs in improving the inelastic earthquake response of a 10-story frame structure.

1. Introduction

Control systems are occasionally used and installed in buildings to improve the structural system's resilience against strong winds and earthquakes. Resilience refers to absorbing or avoiding damage without suffering from complete failure. The book of Soong and Constantinou [1] introduces structural control systems' fundamental concepts and their application in buildings. They define three main groups of structural control systems: (i) active, (ii) semi-active, and (iii) passive. Although around the early 90 s, extensive analytical and experimental research has been conducted on active control systems (e.g., [2,3,4]), considerations such as cost-effectiveness and reliability have limited their acceptance among civil engineers [5].

A passive control system is defined as a system that does not require an external power source for operation. It utilizes the structure's motion to develop the control forces (base isolation system, friction damper, metallic yield damper, buckling-restraint-brace, fluid viscous dampers, etc.). Passive control systems' appealing characteristics are their long-term reliability, stable energy dissipation performance, and not require an external power supply. Because of these attractive properties, passive control systems have been implemented in civil structures around the world (e.g., [6–16]).

A semi-active control system may be defined as a system that typically requires a small external power source for operation and utilizes the structure's motion to develop the control forces, whose magnitude is to be adjusted by the external power source [2]. Compared to an active control system, a semi-active control system does not require a functional computer during the dynamic excitation to run the control algorithm and actuators, which feed on high power. Compared to a passive control system, the semi-active control forces are generated based on feedback from sensors rather than its motion – giving it the ability to adapt under wind load and earthquake load and the ability to control more than one type of dynamic response (e.g., [17–19]).

* Corresponding author.
E-mail address: assafs@bgu.ac.il (A. Shmerling).

https://doi.org/10.1016/j.compstruc.2023.107032
0045-7949/

Semi-active systems have been implemented in full-scale experimental structures, buildings, and bridges. Ikeda [20] lists numerous semi-active system applications for tall buildings in Japan between 1990 and 2006. The recent review papers on control devices by Saaed et al. [21] and Lu et al. [22] show that additional semi-active systems have experimented on small-scale benchmark structures. That includes the semi-active tuned mass damper, semi-active tuned liquid damper, semi-active friction damper, semi-active vibration absorber, adaptive stiffness device, electrorheological damper, and semi-active fluid viscous damper (SAFVDs). This paper is concerned with developing a practical algorithm for SAFVDs based on acceleration measurements.

The operation of a SAFVD device is similar to that of a passive fluid viscous damper except that, based on the status of the control valve, it can deliver damping at two distinct levels (two-stage) or over a wide range between an upper and lower bound (continuously adjustable). The first study on a two-stage SAFVD has been presented by Shinozuka et al. [23]. In their study, they modified the passive device by allowing for the development of stiffness through the removal of the accumulator. Symans et al. [24] developed a continuously adjustable SAFVD using a control valve connected to an external accumulator that regulates the volume of hydraulic fluid inside the damper. Further study on the application and effects on the dynamic response of Symans et al. [24] SAFVD device is provided in [25] and [26], respectively. Zhang and Agrawal [27] introduced a hybrid controller that combines a passive component, which responds to the frequency of the vibration, with a semi-active feature, which reacts to the amplitude. The experimental results show that the proposed controller can reduce the peak amplitude of the vibration by up to 80% compared to a passive controller.

Numerous researchers have developed control strategies for regulating the command voltage applied to the SAFVD of Symans et al. [24] to adjust the fluid flow optimally. Reigles and Symans [28] utilized a supervisory fuzzy logic control algorithm to derive the optimal control law and used the device to reinforce elastomeric base-isolation bearings. The control algorithm refers to the Laplace-domain transfer function of the static and transient response under a step function command voltage and accounts for the initial static delay. Waghmare et al. [29] implemented the SAFVD in multistory frame structures and used the clipped control algorithm to yield the control law. Another work is that of Bakhshinezhad and Mohebbi [30], which introduces a genetic algorithm to determine the optimal change in the damping coefficient. Shi et al. [31] aim to reduce bridge cables' response to wind-induced vibrations. The developed control scheme modifies the stiffness and damping of the cables based on closed-loop feedback on the bridge response. Also, the control approach uses negative stiffness as a counterintuitive approach that involves adding a component to the system that acts in the opposite direction to the cable displacement. This negative stiffness is combined with a semi-active viscous damping system to achieve a fully tracking active control force.

Control strategies designated to other system types can also be utilized for SAFVD implementation. Xu et al. [32] suggest a semi-active control strategy that adds an active isolation element that can adjust the damping components of a passive base isolation system in real-time based on lateral deformation. Earthquake simulations show that the control strategy enhances dynamic performance. Ying et al. [33] formulated a stochastic optimal control problem where the earthquake response and energy consumption by magnetorheological damper are regulated simultaneously. The derived optimal control law proves its effectiveness compared to other control strategies. Vu et al. [34] utilized a nonlinear inhomogeneous optimal control approach, which adjusts the stiffness and damping of the active isolation element based on the lateral motion to the seismic load. The objective of the control strategy is to minimize the structural response while minimizing the energy consumed by the active isolation element. The earthquake simulations demonstrate the efficacy of the algorithm in reducing energy consumption. While all the above strategies proved efficient, they are suitable for structures whose dynamic response remains about the elastic range due to the linear-elastic equation of motion and address stochastic noise. This paper addresses inelastic frame structures and modifies the SAFVD regarding real-time deterministic signals. Moreover, the methodology refers to a short-horizon problem and uses a prediction model to cope with the time delays.

2. SAFVD assembly

The SAFVD developed and proposed by Symans et al. [24] is depicted in Fig. 1. The damper consists of a stainless steel cylinder containing a piston with an orifice head and an accumulator. The cylinder comprises thin silicone oil with a kinematic viscosity of about 100 mm^2/s. The orifice flow is subject to a passive bi-metallic thermostat that allows stable operation of the device over a wide temperature range from −40℃ to 70℃. The SAFVD force generated results from a pressure differential across the piston head. The orifice within the passive device utilizes specially shaped passages to alter flow characteristics with fluid speed. The force output is proportional to the velocity of the piston head relative to the damper housing. That results in essentially linear viscous behavior.

The damper's semi-activity comes into play by an external fluid flow path created by drilling two ports in the cylindrical housing and connecting them with steel tubing and a control valve. The orifice opening within the control valve determines the fluid passing through the external path. High damping capability is when the control valve is closed, and low damping capability is when the control valve is open. Obtaining an intermediate level of damping is when the control valve is positioned between open and closed. The damping force of the SAFVD is given by:

$$u\left(\xi,\dot{d}\right) = c(\xi)\dot{d}(t) \quad \leftrightarrow \quad c^{min} \le c(\xi) \le c^{max} \tag{1}$$

where c is the damping coefficient, ξ is the command voltage, and $\dot{d}$ is the relative velocity of the piston head. The coefficient c is bounded by a maximum c^{max} and a minimum c^{min} value and may take on any matter within these bounds.

The damping characteristics of the SAFVD are generally a function of command voltage. That is demonstrated in Symans et al. [24] for a damper experimented for valve opening under a command signal from 0 to 3 V. They suggest the following expression for the damping coefficient:

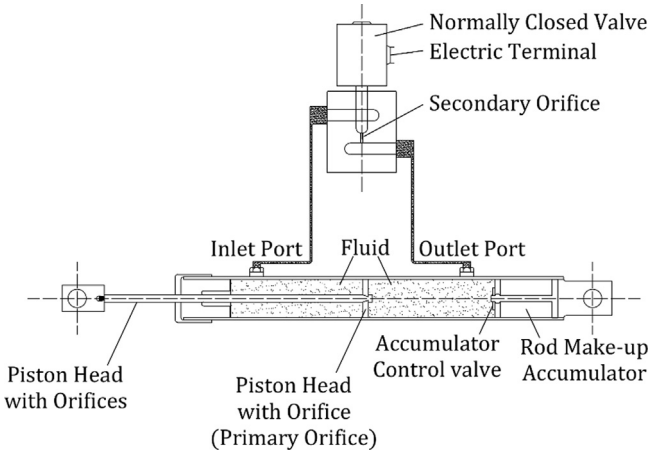

Fig. 1. Semi-active fluid damper ensemble.

$$c(\xi) = c^{min} + \left(c^{max} - c^{min}\right)\exp\left(-\alpha\xi^{\eta}\right) \quad \leftrightarrow \quad \xi(t) \geq 0 \tag{2}$$

where α (units: volt$^{-\eta}$) and η are constant parameters. The energy capabilities of the system depend on the type of hydraulic fluid. Nevertheless, the system is sustainable for typical hydraulic oil and requires maintenance every two decades.

3. Lateral force equilibrium

The SAFVD control scheme is formulated and developed using the matrix equations model of inelastic frame structure under lateral movements. The control strategy uses closed-loop feedback regarding the lateral motion in the SAFVD plane; thus, the matrix equations only refer to plane frame models. Also, it is assumed that the service, dead, and gravitational loads applied to the ceilings and transferred to the frame's beams are modeled as lumped mass at the beam's span center. Accordingly, the lateral force equilibrium governing the frame structure's movement under earthquake excitation is expressed by:

$$\begin{aligned} &\mathbf{f}^{I}(t) + \mathbf{f}^{R}\left(\dot{\mathbf{f}}^{R}, \dot{\mathbf{d}}, t\right) + \mathbf{f}^{D}(t) = \mathbf{u}\left(\xi, \dot{\mathbf{d}}\right) \\ &\text{and :} \\ &\mathbf{d}(0) = 0 \\ &\dot{\mathbf{d}}(0) = 0 \\ &\mathbf{f}^{R}(0,0,0) = 0 \end{aligned} \tag{3}$$

where $\mathbf{f}^{I} \in \mathbb{R}^{N}$ is the inertia force vector, $\mathbf{f}^{R} \in \mathbb{R}^{N}$ is the inelastic columns' resisting force vector, $\mathbf{f}^{D} \in \mathbb{R}^{N}$ vector represents the lateral force induced by the structure's inherent damping, and $\mathbf{u} \in \mathbb{R}^{N}$ is the SAFVD control force vector. Eq. (3) does not refer to an explicit load vector. Instead, in the case of earthquake excitation, the effective load stems from the inertia force.

The frame structure's lateral deformations are addressed in displacement and drift coordinates. Fig. 2(a) depicts the ground displacement d_g, Fig. 2(b) shows the interstory drift deformations and relative-to-ground displacements, and Fig. 2(c) illustrates the total displacements. The interstory drift deformation between the mass n^{th} and the *n-1* mass is denoted by d_n – relating to the lateral mass displacement vector as:

$$\begin{aligned} &\mathbf{x}(t) = \mathbf{T}_{d\to x}\mathbf{d}(t) \quad \leftrightarrow \quad \mathbf{x}(t) = \begin{bmatrix} x(t)_1 \\ \vdots \\ x(t)_N \end{bmatrix}; \quad \mathbf{T}_{d\to x} = \begin{bmatrix} 1 & 0 & \\ \vdots & \ddots & \\ 1 & \cdots & 1 \end{bmatrix}; \\ &\mathbf{d} = \begin{bmatrix} d(t)_1 \\ \vdots \\ d(t)_N \end{bmatrix} \end{aligned} \tag{4}$$

where $\mathbf{x} \in \mathbb{R}^{N}$ is the lateral mass displacements vector, $\mathbf{d} \in \mathbb{R}^{N}$ is the interstory drift deformations vector, and $\mathbf{T}_{d\to x} \in \mathbb{R}^{N} \times \mathbb{R}^{N}$ is the transformation matrix from drift coordinates into displacement coordinates. The total lateral displacement function is:

$$\mathbf{x}^{tot}(t) = \mathbf{1}d_g(t) + \mathbf{T}_{d\to x}\mathbf{d}(t) \quad \leftrightarrow \quad \ldots \mathbf{1} = \begin{bmatrix} 1 \\ \vdots \\ 1 \end{bmatrix}; \quad \mathbf{x}^{tot}(t) = \begin{bmatrix} x_1^{tot}(t) \\ \vdots \\ x_N^{tot}(t) \end{bmatrix} \tag{5}$$

The inertia force relates to the total acceleration applied to the lumped masses. Denote the second time-derivates $\ddot{d}_g(t)$ and $\ddot{\mathbf{x}}^{tot}(t) \in \mathbb{R}^{N}$ as $a_g(t)$ and $\mathbf{a}^{tot}(t) \in \mathbb{R}^{N}$, respectively, where $a_g(t)$ is referred to henceforth as the ground acceleration and $\boldsymbol{a}^{tot}(t)$ is the total accelerations vector. Then, according to Newton's second law of motion, the inertia force is:

$$\begin{aligned} &\mathbf{f}^{I}(t) = (\mathbf{T}_{d\to x})'\mathbf{M}_{\mathbf{x}}\mathbf{a}^{tot}(t) = \begin{bmatrix} f_1^{I}(t) \\ \vdots \\ f_N^{I}(t) \end{bmatrix} \\ &\mathbf{a}^{tot}(t) = \mathbf{1}a_g(t) + \mathbf{T}_{d\to x}\,\mathbf{d}\,(t) = \begin{bmatrix} a_1^{tot}(t) \\ \vdots \\ a_N^{tot}(t) \end{bmatrix} \end{aligned} \tag{6}$$

where $(\ )'$ denotes the matrix transpose, and $\mathbf{M}_{\mathbf{x}} \in \mathbb{R}^{N} \times \mathbb{R}^{N}$ is the mass matrix in displacement coordinates. In the case of lumped masses, $\mathbf{M}_{\mathbf{x}}$ is diagonal and composed of the applied mass quantities. That is:

$$\mathbf{M}_{\mathbf{x}} = \begin{bmatrix} m_1 & & \\ & \ddots & \\ & & m_N \end{bmatrix} \tag{7}$$

Where m_n is the nth story lumped mass.

c vector $\mathbf{f}^{R}$ is assumed to be hysteretic so that it is equal to the time integration of its rate $\dot{\mathbf{f}}^{R} \in \mathbb{R}^{N}$. That is:

$$\begin{aligned} &\mathbf{f}^{R}\left(\dot{\mathbf{f}}^{R}, \dot{\mathbf{d}}, t\right) = \int_0^t \dot{\mathbf{f}}^{R}\left(\mathbf{f}^{R}, \dot{\mathbf{d}}, \tau\right)d\tau = \int_0^t \mathbf{K}_d\left(\mathbf{f}^{R}, \dot{\mathbf{d}}, \tau\right)\dot{\mathbf{d}}(\tau)d\tau \\ &\qquad\qquad \leftrightarrow \qquad\qquad \ldots \\ &\mathbf{f}^{R}\left(\dot{\mathbf{f}}^{R}, \dot{\mathbf{d}}, t\right) = \begin{bmatrix} f_1^{R}\left(f_1^{R}, \dot{d}_1, t\right) \\ \vdots \\ f_N^{R}\left(f_N^{R}, \dot{d}_N, t\right) \end{bmatrix} \end{aligned} \tag{8}$$

where $\mathbf{K}_d \in \mathbb{R}^{N} \times \mathbb{R}^{N}$ is the tangent stiffness in drift coordinates and is assumed to be dependent on $\mathbf{f}^{R}$, $\mathbf{d}$, and $\dot{\mathbf{d}} \in \mathbb{R}^{N}$ – making the determination and calculation of $\mathbf{f}^{R}$ implicit. The inherent damping force vector $\mathbf{f}^{D}$ is defined by:

$$\mathbf{f}^{D}(t) = \mathbf{C}_d\dot{\mathbf{d}}(t) = \begin{bmatrix} f_1^{D}(t) \\ \vdots \\ f_N^{D}(t) \end{bmatrix} \tag{9}$$

where $\mathbf{C}_d \in \mathbb{R}^{N} \times \mathbb{R}^{N}$ is a classical inherent damping matrix and is calculated using Caughey's classical damping equation:

$$\mathbf{C}_d = \mathbf{M}_d\left(\sum_{v=1}^{N} 2\zeta\omega_v/\left(\phi_v{}^{T}\mathbf{M}_d\phi_v\right)\phi_v\phi_v{}^{T}\right)\mathbf{M}_d \in \mathbb{R}^{N} \times \mathbb{R}^{N} \tag{10}$$

So that ω_v denotes the v^{th} mode frequency, $\phi_v \in \mathbb{R}^{N}$ denotes the v^{th} mode-shape vector, and ζ is the inherent damping ratio. The eigenvalues problem that derives the modal properties is:

$$\begin{aligned} &\det\left|\mathbf{M}_d{}^{-1}\mathbf{K}_d(0,0,0) - \omega_v{}^2\mathbf{I}\right| = 0 \quad \leftrightarrow \quad \cdots \\ &\omega_1 < \cdots < \omega_v < \cdots \omega_N \end{aligned} \tag{11}$$

$$\left(\mathbf{M}_d{}^{-1}\mathbf{K}_d(0,0,0) - \omega_v{}^2\mathbf{I}\right)\phi_v = 0 \quad \forall \quad v = 1, \cdots, N \tag{12}$$

Here, the matrix $\mathbf{I} \in \mathbb{R}^{N} \times \mathbb{R}^{N}$ is the identity matrix and $\mathbf{K}_d(0,0,0) \in \mathbb{R}^{N} \times \mathbb{R}^{N}$ represents the frame structure's stiffness matrix at the initial time with no stiffness and strength degradations.

Substituting Eqs. (6) and (9) into the lateral force equilibrium of Eq. (3) yields the following representation for lateral force equilibrium:

$$\mathbf{f}^{R}\left(\dot{\mathbf{f}}^{R},\dot{\mathbf{d}},t\right)+\mathbf{C}_{d}\dot{\mathbf{d}}(t)-\mathbf{u}\left(\xi,\dot{\mathbf{d}}\right)=-(\mathbf{T}_{d\to x})'\mathbf{M}_{\mathbf{x}}\mathbf{a}^{tot}(t)=-\mathbf{f}^{I}(t) \tag{13}$$

The combination of Eq. (13) left-hand side forces yields the shear force applied to the frame structure's columns. Hence, $-\mathbf{f}^{I}$ also represents the shear force vector. Assuming the components of $\mathbf{M}_{\mathbf{x}}$ are known, the vector $\mathbf{f}^{I}$ is measurable by using accelerometer readings to get $\mathbf{a}^{tot}$. The control strategy is to have the SAFVD force vector $\mathbf{u}$ using the readings of $\mathbf{a}^{tot}$ to reduce it and, accordingly, reduce the shear force applied to the columns.

The SAFVD force in vector form $\mathbf{u}$ is defined after Eq. (1) scalar term and is expressed as:

$$\begin{aligned}&\mathbf{u}\left(\xi,\dot{\mathbf{d}}\right)=-\mathbf{c}(\xi)\dot{\mathbf{d}}(t)=\begin{bmatrix}u_1\left(\xi_1,\dot{d}_1\right)\\ \vdots\\ u_N\left(\xi_N,\dot{d}_N\right)\end{bmatrix}\\ &\text{and}:\\ &\mathbf{c}(\xi)=\begin{bmatrix}c_1(\xi_1) & & \\ & \ddots & \\ & & c_N(\xi_N)\end{bmatrix}\\ &c_n(\xi_n)=c_n^{min}+\left(c_n^{max}-c_n^{min}\right)\exp\left\{-\alpha(\xi_n(t))^{\eta}\right\}\\ &\qquad\leftrightarrow c_n^{min}\le c_n(\xi_n)\le c_n^{max};\qquad\qquad \xi_n(t)\ge 0\end{aligned} \tag{14}$$

Where u_n, c_n, ξ_n, c_n^{min}, and c_n^{max} are the nth story's force, damping coefficient, voltage, and min/max boundaries, respectively. This paper's control strategy looks to define ξ_n to regulate $-f_n^I$, for each $n=1,\cdots,N$ story, and result in smaller shear forces. Since the control force employs the readings of $\mathbf{a}^{tot}$, the control problem addresses a short-horizon discrete scheme to define ξ_n at each time step.

4. Short-horizon problem

The SAFVD control strategy minimizes the columns' shear forces while referring to the total acceleration and the SAFVD force magnitudes. That is applicable through the following equality:

$$\min\left\{\mathbf{f}^{R}\left(\dot{\mathbf{f}}^{R},\dot{\mathbf{d}},t\right)+\mathbf{C}_{d}\dot{\mathbf{d}}(t)\right\}\equiv\min\left\{-\mathbf{T}'_{d\to x}\mathbf{M}_{\mathbf{x}}\mathbf{a}^{tot}(t)+\mathbf{u}\left(\xi,\dot{\mathbf{d}}\right)\right\} \tag{15}$$

The shear forces minimization is addressed in squared form as a short-horizon problem comprising the corresponding objective function subject to the lateral force equilibrium and command voltage change limitation. That is:

$$\left.\begin{aligned}&\min_{\Delta\xi_i}\quad\left\{J_i=\Delta\mathbf{a}_i^{tot\prime}\mathbf{Q}\Delta\mathbf{a}_i^{tot}-2\Delta\mathbf{a}_i^{tot\prime}\mathbf{R}\Delta\mathbf{u}_i+\Delta\mathbf{u}_i{}'\Delta\mathbf{u}_i\right\}\\ &\text{and:}\quad\Delta\mathbf{a}_i^{tot}=\mathbf{a}_i^{tot}-\mathbf{a}_{i-1}^{tot}\\ &\qquad\Delta\mathbf{u}_i=\mathbf{u}_i-\mathbf{u}_{i-1}\\ &\qquad\mathbf{Q}=\mathbf{M}_{\mathbf{x}}'\mathbf{T}_{d\to x}\mathbf{T}'_{d\to x}\mathbf{M}_{\mathbf{x}}\\ &\qquad\mathbf{R}=\mathbf{M}_{\mathbf{x}}'\mathbf{T}_{d\to x}\\ &\text{s.t.}\quad\mathbf{f}_i^{R}+\mathbf{C}_d\dot{\mathbf{d}}_i+\mathbf{T}'_{d\to x}\mathbf{M}_{\mathbf{x}}\,\mathbf{a}_i^{tot}-\mathbf{u}_i=\mathbf{0}\\ &\qquad|\Delta\xi_i|\le\Delta\xi^{max}\end{aligned}\right\}\quad\forall\quad i=1,\dots,\tfrac{t_f}{\Delta t} \tag{16}$$

The objective function minimizes the incremental increase in shear forces over a short time step Δt where i represents the time index $i=0,1,2,\cdots,\frac{t_f}{\Delta t}$ and a scalar/vector/matrix, for example $\mathbf{u}$, at $t=i\Delta t$ is denoted as $\mathbf{u}_i$. The ith step $\mathbf{u}_i$ and $\mathbf{c}_i$ are defined by:

$$\left.\begin{aligned}&\mathbf{u}_i=-\mathbf{c}_i\dot{\mathbf{d}}_i\\ &\text{and}:\\ &\mathbf{c}_i=\begin{bmatrix}c_{1,i} & & \\ & \ddots & \\ & & c_{N,i}\end{bmatrix}\\ &c_{n,i}=c_n^{min}+\left(c_n^{max}-c_n^{min}\right)\exp\left\{-\alpha(\xi_{n,i})^{\eta}\right\}\\ &c_n^{min}\le c_{n,i}\le c_n^{max};\quad\xi_{n,i}\ge 0\end{aligned}\right\}\quad\forall\quad i=0,1,\cdots,\tfrac{t_f}{\Delta t} \tag{17}$$

Eq. (16) is solved using the method of Lagrange multipliers. Accordingly, the associated Lagrangian function:

$$\begin{aligned}L_i=&\Delta\mathbf{a}_i^{tot\prime}\mathbf{Q}\Delta\mathbf{a}_i^{tot}-2\Delta\mathbf{a}_i^{tot\prime}\mathbf{R}\Delta\mathbf{u}_i+\Delta\mathbf{u}_i{}'\Delta\mathbf{u}_i\\ &+\lambda_i'\left(\mathbf{f}_i^{R}+\mathbf{f}_i^{D}+\mathbf{T}'_{d\to x}\mathbf{M}_{\mathbf{x}}\mathbf{a}_i^{tot}-\mathbf{u}_i\right)\qquad\forall\quad i=1,\cdots,\tfrac{t_f}{\Delta t}\end{aligned} \tag{18}$$

and the optimality conditions:

$$\left.\begin{aligned}&\tfrac{\partial L_i}{\partial\mathbf{u}_i}=-2\mathbf{R}\Delta\mathbf{a}_i^{tot}+2\Delta\mathbf{u}_i-\lambda_i=0\\ &\tfrac{\partial L_i}{\partial\mathbf{a}_i^{tot}}=2\mathbf{Q}\Delta\mathbf{a}_i^{tot}-2\mathbf{R}\Delta\mathbf{u}_i+\mathbf{T}'_{d\to x}\mathbf{M}_{\mathbf{x}}\lambda_i=0\end{aligned}\right\}\quad\forall\quad i=1,\cdots,\tfrac{t_f}{\Delta t} \tag{19}$$

Where $\lambda_i\in\mathbb{R}^N$ is the Lagrange multipliers vector. The optimization conditions of Eq. (19) lead to the following optimal change in SAFVD force:

$$\Delta\mathbf{u}_i=\left(\mathbf{T}'_{d\to x}\mathbf{M}_{\mathbf{x}}-\mathbf{R}\right)^{-1}\left(\mathbf{Q}-\mathbf{T}'_{d\to x}\mathbf{M}_{\mathbf{x}}\mathbf{R}\right)\Delta\mathbf{a}_i^{tot}\quad\forall\quad i=1,\cdots,\tfrac{t_f}{\Delta t} \tag{20}$$

The ith step change in the nth story SAFVD force $\Delta u_{n,i}$ is proportional to the change in command voltage by the exponent term:

$$\begin{aligned}\Delta u_{n,i}=&\left(c_n^{max}-c_n^{min}\right)\left(\exp\left\{-\alpha\left(\xi_{n,i-1}+\Delta\xi_{n,i}\right)^{\eta}\right\}\right.\\ &\left.-\exp\left\{-\alpha\left(\xi_{n,i-1}\right)^{\eta}\right\}\right)\forall n=1,\cdots,N\end{aligned} \tag{21}$$

Where $\Delta\xi_{n,i}$ is the nth story change in command voltage at the ith time step. Since the function of $\Delta\xi_{n,i}$ by $\Delta u_{n,i}$ is implicit, we define the shift in command voltage by:

$$\Delta\xi_i=\text{sign}(u_i\odot\Delta u_i)\Delta\xi^{max} \tag{22}$$

Where $\Delta\xi^{max}$ is taken from Eq. (16) and represents the maximum change in command voltage for each step.

The change $\Delta\mathbf{u}_i$ is expressed by ith total acceleration reading $\mathbf{a}_i^{tot}$ – measured by accelerometers. However, $\Delta\mathbf{u}_i$ and $\Delta\xi_i$ are decided and induced into the structure before $\mathbf{a}_i^{tot}$ occurs and measures. Accordingly, the Kalman filter is employed to define $\Delta\xi_i$ by an estimation of $\mathbf{a}_i^{tot}$.

5. Prediction model

The Kalman filter prediction model posterizes the next step's acceleration reading using the two latest known measurements. While referring to previous acceleration quantities by Kalman filter, instead of referring to the structure's dynamics, may provide lower estimation, the prediction scheme is applicable under circumstances where, for example, the inelastic properties are uncertain. The total acceleration evaluation uses the central difference scheme and is of the form:

$$\mathbf{a}_i^{tot}\cong\mathbf{a}_{i-1}^{tot}+\Delta t\tfrac{\mathbf{a}_i^{tot}-\mathbf{a}_{i-2}^{tot}}{2\Delta t}\quad\forall\quad i=1,2,\cdots,\tfrac{t_f}{\Delta t}\quad\&\quad\mathbf{a}_{-1}^{tot}=0 \tag{23}$$

which yields the following measuring model:

$$\mathbf{z}_i=\mathbf{A}\mathbf{z}_{i-1}+\mathbf{E}_i^{z}\quad\leftrightarrow\quad\mathbf{E}_i^{z}\,\mathcal{N}(0,\Sigma^{z});\quad\Sigma^{z}=\sigma^{z}\sigma^{z\prime} \tag{24}$$

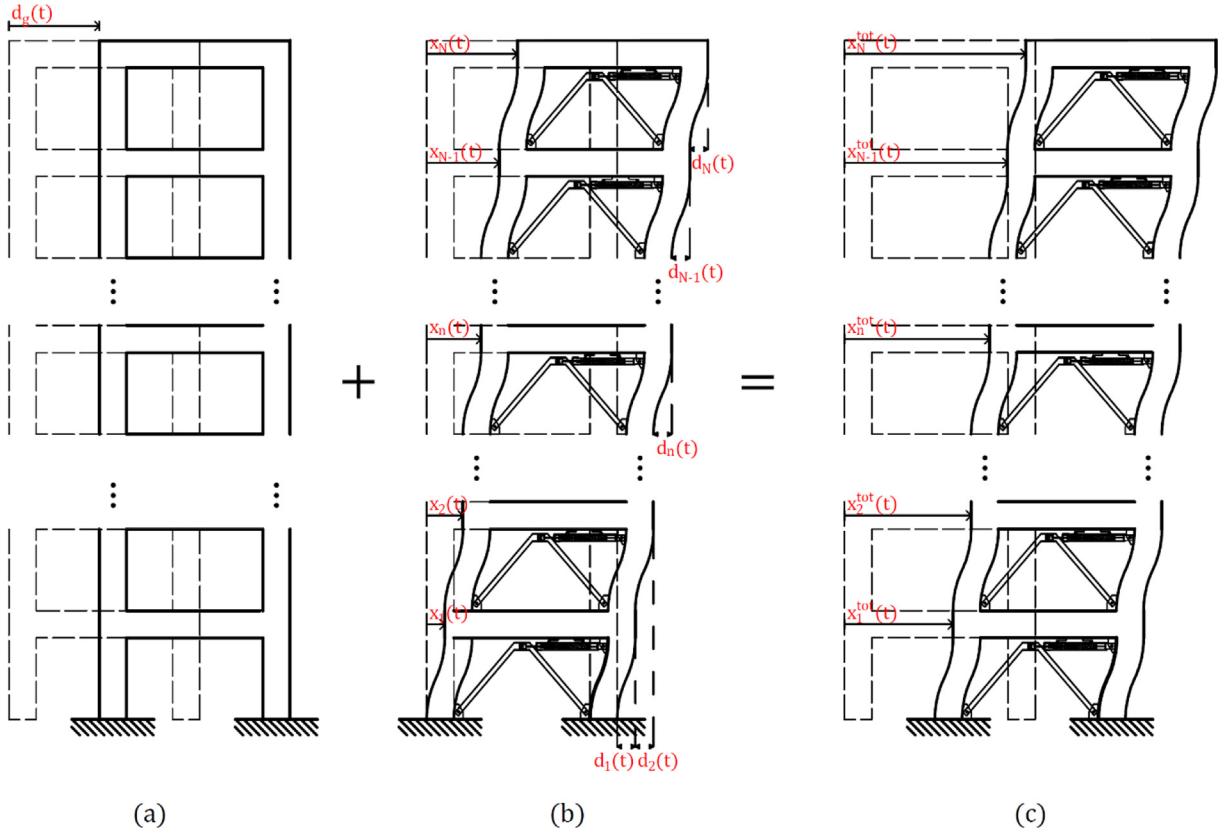

Fig. 2. Frame structure's deformations and displacements: (**a**) ground displacement, (**b**) structural displacement and interstory drift deformations, (**c**) total displacements.

$$\mathbf{a}_i^{tot} = \mathbf{C}\mathbf{z}_i + \mathbf{E}_i^y \quad \leftrightarrow \quad \mathbf{E}_i^y \sim \mathcal{N}(0, \Sigma^y); \quad \Sigma^y = \sigma^y \sigma^{y\prime} \tag{25}$$

Here, $\mathbf{E}_i^z \in \mathbb{R}^{2N}$ is the stochastic error regarding $\mathbf{z}_i \in \mathbb{R}^{2N}$, $\Sigma^z \in \mathbb{R}^{2N} \times \mathbb{R}^{2N}$ is the covariance matrix of $\mathbf{E}_i^z$, $\sigma^z \in \mathbb{R}^{2N}$ is the variance vector of $\mathbf{E}_i^z$, $\mathbf{E}_i^y \in \mathbb{R}^N$ is the stochastic error in the output measurements of $\mathbf{a}_i^{tot}$, $\Sigma^y \in \mathbb{R}^N \times \mathbb{R}^N$ is the covariance matrix of $\mathbf{E}_i^y$, and $\sigma^y \in \mathbb{R}^N$ is the variance vector of $\mathbf{E}_i^y$. The vector $\mathbf{z}_i$ is defined by:

$$\mathbf{z}_i = \begin{bmatrix} -\mathbf{a}_{i-1}^{tot} \\ \mathbf{a}_i^{tot} \end{bmatrix} \tag{26}$$

and the matrices $\mathbf{A} \in \mathbb{R}^{2N} \times \mathbb{R}^{2N}$ and $\mathbf{C} \in \mathbb{R}^N \times \mathbb{R}^{2N}$ are:

$$\mathbf{A} = \begin{bmatrix} 0 & \mathbf{I} \\ \mathbf{I} & 2\mathbf{I} \end{bmatrix}; \quad \mathbf{C} = [0 \quad \mathbf{I}] \tag{27}$$

The Kalman filter estimates $\mathbf{z}_i$ and $\mathbf{a}_i^{tot}$ by:

$$\hat{\mathbf{z}}_i = \mathbf{A}\hat{\mathbf{z}}_{i-1} + \mathcal{K}_i\left(\mathbf{a}_i^{tot} - \hat{\mathbf{a}}_i^{tot}\right) \tag{28}$$

$$\mathbf{a}_i^{tot} = \mathbf{C}\hat{\mathbf{z}}_i \tag{29}$$

So that $\mathcal{K}_i \in \mathbb{R}^N \times \mathbb{R}^N$ is the i^{th} Kalman filter gain, $\hat{\mathbf{a}}_i^{tot} \in \mathbb{R}^N$ denotes the estimation of $\mathbf{a}_i^{tot}$, and $\hat{\mathbf{z}}_i \in \mathbb{R}^{2N}$ denotes the estimation of $\mathbf{z}_i$.

The control strategy presented above employs the Kalman filter model in estimating the acceleration at the subsequent time step. The proposed Kalman model corresponds to the closed-loop scheme depicted in Fig. 3. The model does not regard the earthquake input directly but rather the structural response. Accordingly, The Kalman algorithm corresponding to the prediction model is employed to assess $\mathbf{a}_i^{tot}$ through $\hat{\mathbf{a}}_i^{tot}$. The algorithm consists of the following two stages and five calculation steps.

5.1. Prediction stage

Calculate the apriori estimate $\hat{\mathbf{z}}_i^{tot-} \in \mathbb{R}^{2N}$ by:

$$\hat{\mathbf{z}}_i^{tot-} = \mathbf{A}\hat{\mathbf{z}}_{i-1}^{tot} \tag{30a}$$

Then, determine the apriori estimate error covariance matrix $\mathbf{P}_i^- \in \mathbb{R}^{2N} \times \mathbb{R}^{2N}$:

$$\mathbf{P}_i^- = \mathbf{A}\mathbf{P}_{i-1}\mathbf{A}' + \Sigma^z \tag{30b}$$

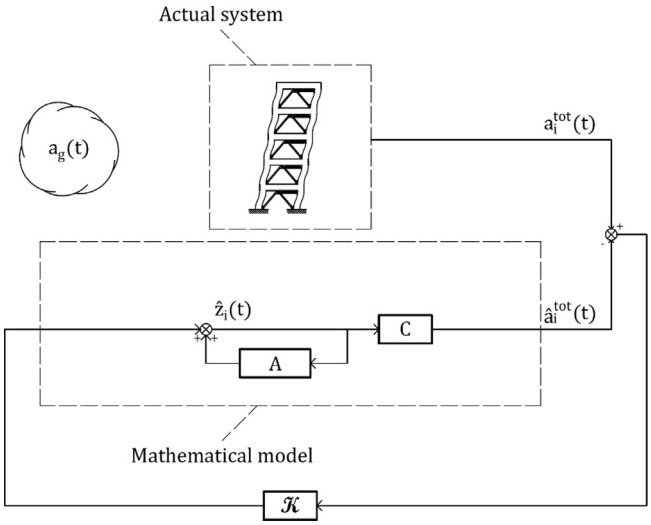

Fig. 3. Proposed Kalman filter model.

5.2. Update stage

Derive the ith Kalman gain $\mathscr{K}_i$ using the expression:

$$\mathscr{K}_i = \mathbf{P}_i^- \mathbf{C}' \left(\mathbf{C}\mathbf{P}_i^- \mathbf{C}' + \Sigma^y\right)^{-1} \tag{30c}$$

Calculate the posterior estimate:

$$\widehat{\mathbf{a}}_i^{tot} = \widehat{\mathbf{a}}_i^{tot-} + \mathscr{K}_i \left(\mathbf{y}_i - \mathbf{C}\widehat{\mathbf{a}}_i^{tot-}\right) \tag{30d}$$

Determine the posterior estimate error covariance $\mathbf{P}_i \in \mathbb{R}^{2N} \times \mathbb{R}^{2N}$

$$\mathbf{P}_i = (\mathbf{I} - \mathscr{K}_i \mathbf{C})\mathbf{P}_i^- \tag{30e}$$

The estimation produced by the Kalman filter significantly depends on the stochastic error covariance matrix. For example, the smaller Σ^z the more the Kalman gain approaches zero. Therefore, the posterior estimate $\widehat{\mathbf{a}}_i^{tot}$ depends on the apriori estimate $\widehat{\mathbf{a}}_i^{tot-}$. On the other hand, The smaller Σ^y the more the Kalman gain approaches the inverse of $\mathbf{C}$ and the posterior estimate depends on the measurement $\mathbf{y}_i$.

Substituting Eq. (20) into Eq. (22) and replacing $\Delta\mathbf{a}_i^{tot}$ with $\widehat{\mathbf{a}}_i^{tot} - \widehat{\mathbf{a}}_{i-1}^{tot}$, the optimal change in command voltage is defined by:

$$\Delta\xi_i = \text{sign}\left(\mathbf{u}_i \odot \left(\left(\mathbf{T}'_{d\to x}\mathbf{M}_\mathbf{x} - \mathbf{R}\right)^{-1}\left(\mathbf{Q} - \mathbf{T}'_{d\to x}\mathbf{M}_\mathbf{x}\mathbf{R}\right)\left(\widehat{\mathbf{a}}_i^{tot} - \widehat{\mathbf{a}}_{i-1}^{tot}\right)\right)\right)\Delta\xi^{max} \tag{31}$$

And, accordingly, the ith command voltage is:

$$\xi_i = \Pi_{[0,\xi^{max}]}(\Delta\xi_{i-1} + \Delta\xi_i) \tag{32}$$

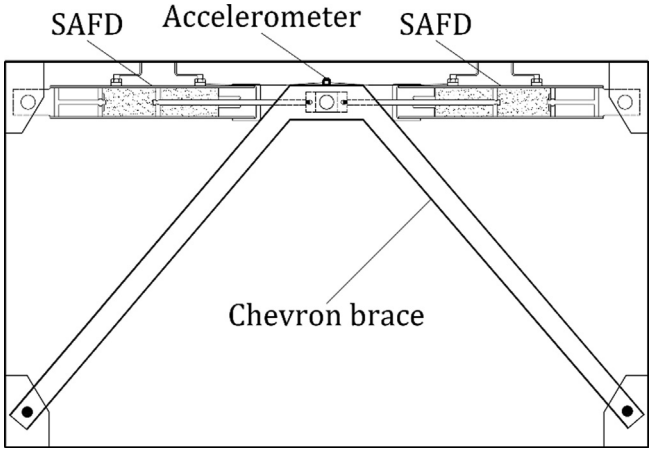

Fig. 4. SAFVD Installation scheme between two columns.

Where $\xi^{max} \in \mathbb{R}^N$ is the maximum possible voltage vector, and the function $\Pi_{[0,\xi^{max}]}(\mathbf{x})$ represents the projection of the vector $\mathbf{x}$ onto the boundaries $[0, \xi^{max}]$ so that:

$$\Pi_{[0,\xi^{max}]}(\mathbf{x}) = \begin{cases} 0, & \text{if} \mathbf{x} < 0 \\ \Delta\xi^{max}, & \text{if} \mathbf{x} > \xi^{max} \\ \mathbf{x}, & \textit{otherwise} \end{cases} = \max\{\min\{\xi^{max}, \mathbf{x}\}, 0\} \tag{33}$$

6. Case study: 10-story high-rise system

The case study deals with regulating the seismic vibrations of a 10-story rigid frame structure whose inelasticity is characterized by the Bouc-Wen hysteretic model regarding $\mathbf{f}^R$. In this case study, the hysteretic model neglects stiffness and strength degradations and assumes that the loading curve (in the elastic regime) and unloading curve are of identical slopes. Accordingly, the Bouc-Wen law of $\mathbf{f}^R$ is given by:

$$\mathbf{f}^R\left(\mathbf{f}^R, \dot{\mathbf{d}}, t\right) = \mathbf{a}\mathbf{k}\mathbf{d}(t) + \int_0^t \mathbf{k}^H\left(\mathbf{f}^R, \dot{\mathbf{d}}, t\right)\dot{\mathbf{d}}(t)dt$$
and:
$$\mathbf{k}^H\left(\mathbf{f}^R, \dot{\mathbf{d}}, t\right) = \begin{bmatrix} k_1^H\left(f_1^R, \dot{d}_1, t\right) & & \\ & \ddots & \\ & & k_N^H\left(f_N^R, \dot{d}_N, t\right) \end{bmatrix}$$
$$k_n^H\left(f_n^H, \dot{d}_n, t\right) = (1-a_n)k_n\left[1 - \left(\frac{f_n^R(t) - a_n k_n d_n(t)}{(1-a_n)f_n^{yld}}\right)^v \left(0.5\text{sign}\left(\dot{d}_n(t)\left(f_n^R(t) - a_n k_n d_n(t)\right)\right) + 0.5\right)\right] \tag{34}$$

Where $\mathbf{k} \in \mathbb{R}^N \times \mathbb{R}^N$ is the diagonal stiffness matrix whose components are the story stiffnesses $k_1, \cdots, k_N$, $\mathbf{a} \in \mathbb{R}^N \times \mathbb{R}^N$ is a diagonal matrix whose components $a_1, \cdots, a_N$ define the ratio between the stories' plastic region stiffness and $k_1, \cdots, k_N$, $\mathbf{k}^H \in \mathbb{R}^N \times \mathbb{R}^N$ is the hysteretic stiffness matrix, and f_n^{yld} is the nth story shear force at first yield. The inelastic parameters are set as follows:

$$\left.\begin{array}{l} \nu = 10 \\ a_n = 0.1 \\ f_n^{yld} = 0.001 H_n k_n \end{array}\right\} \quad \forall \quad n = 1, \cdots, N$$

To better showcase the effectiveness of the SAFVDs, the parameters $a_1, \cdots, a_N$ are set relatively low so that the structure requires more support from the damping force when the resisting force is in its plastic regime.

The SAFVD installation scheme is depicted in Fig. 4. Each span is equipped with two devices using a chevron brace. The device is added to a beam-column system, considering the columns can carry additional shear forces and the span length is sufficient. The absolute acceleration is measured by an accelerometer mounted on the chevron brace. The accelerometer is connected to the control valve, whose voltage commands follow the Kalman filter estimation model and the developed control law. The SAFVD parameters are taken from Symans et al. [24], where $\eta = 3$,

Table 1
Employed earthquake ground acceleration records.

EQ.	Name	Year	Station Name	Mag.	Component	PGA	PGV
						g's	cm/s
1	Denali (Alaska)	2002	TAPS Pump Station #10	7.9	47°Az.	0.33	116
2	Darfield	2010	GDLC	7.0	29E	0.76	116
3			LINC		23E	0.46	109
4	(New Zealand)		ROLC		55 W	0.39	86

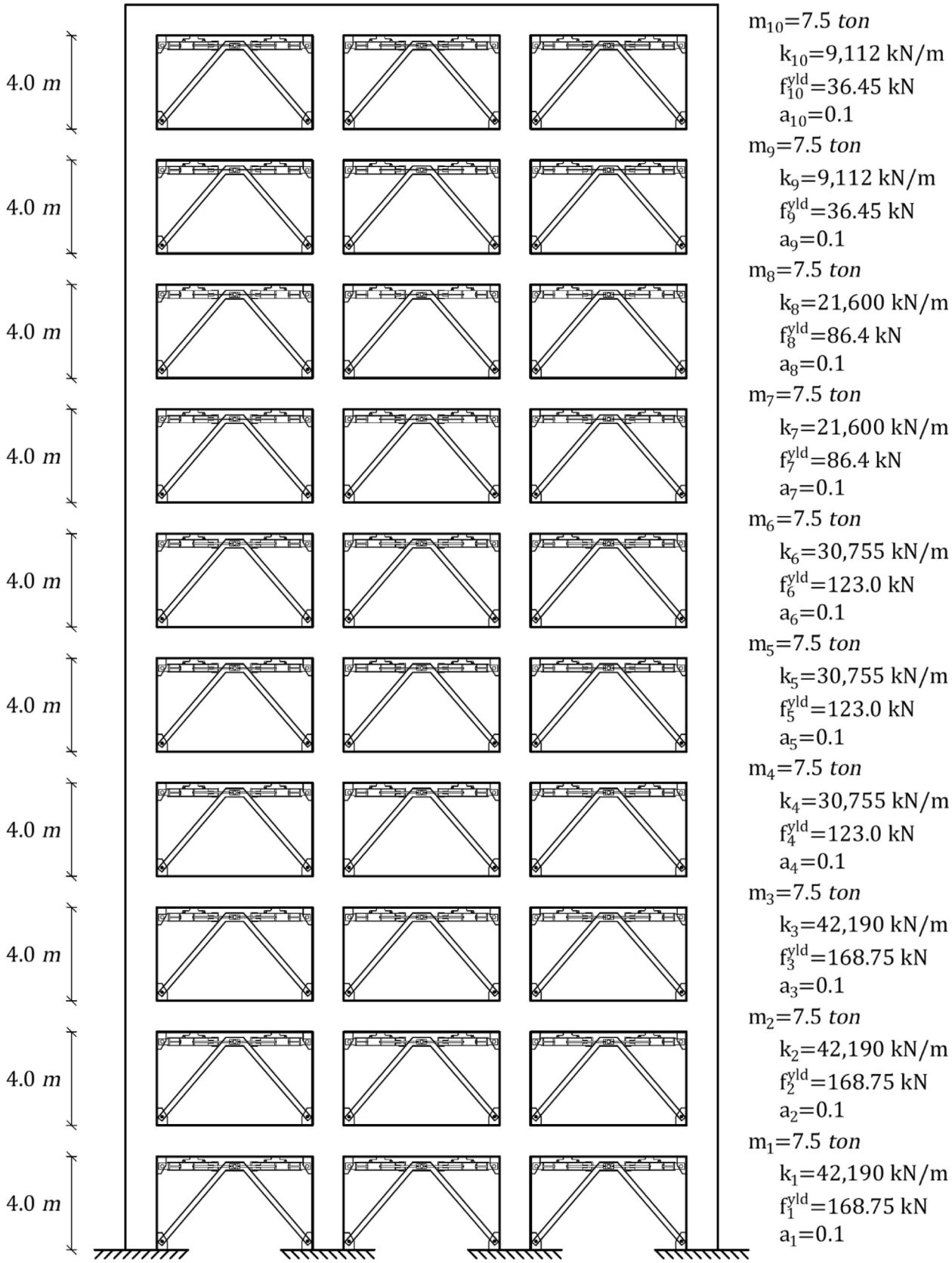

Fig. 5. Elevation scheme of 10-story high-rise system.

$\alpha = 0.4\text{volt}^{-3}$, and $\xi_n^{\max} = 3.0\,\text{volt}$. The maximum/minimum damping coefficients are scaled by 20 to suit the high-rise structure. Hence, $c^{min} = 12 \cdot 2.56\frac{kNs}{m}$, and $c^{\max} = 12 \cdot 17.94\frac{kNs}{m}$.

The case study examines the controlled structure under the four earthquake ground acceleration records specified in Table 1. These records are chosen due to their high PGV, Magnitude, and small

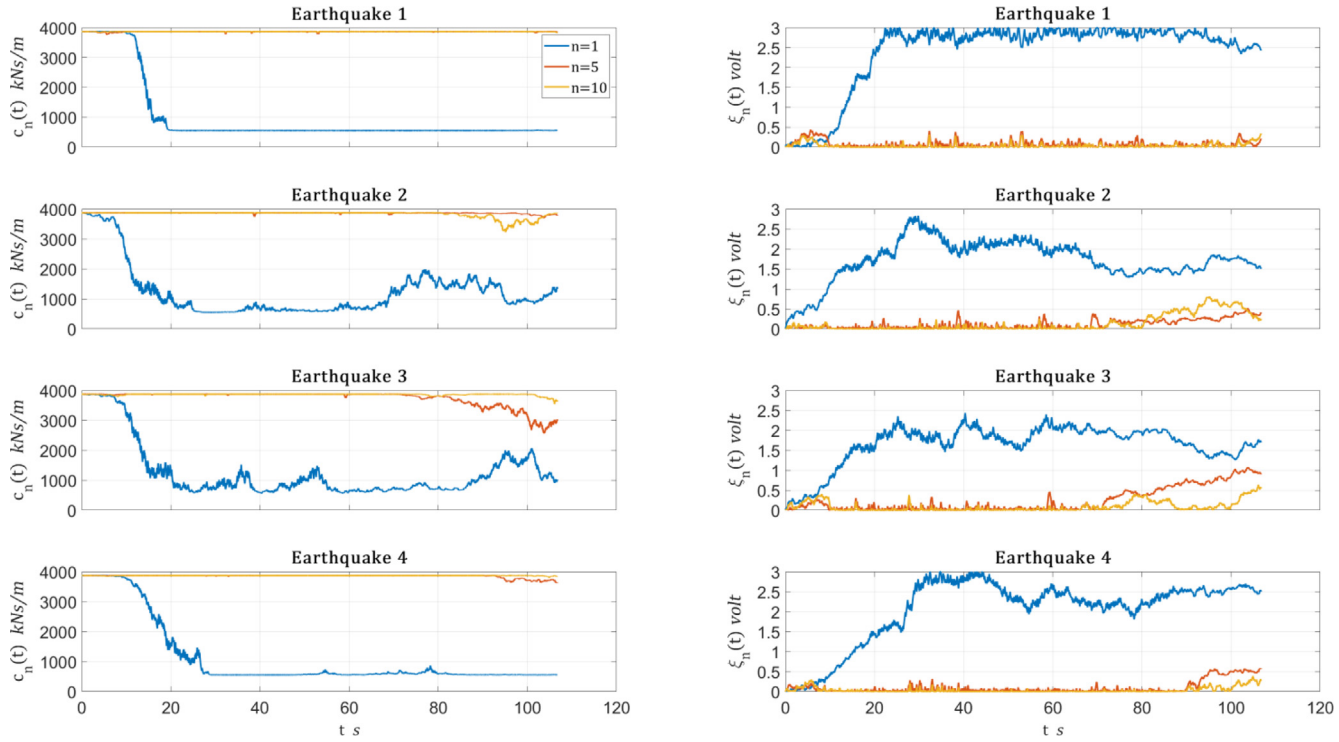

Fig. 6. SAFVD change in damping coefficient and command voltage for stories n = 1,5,10.

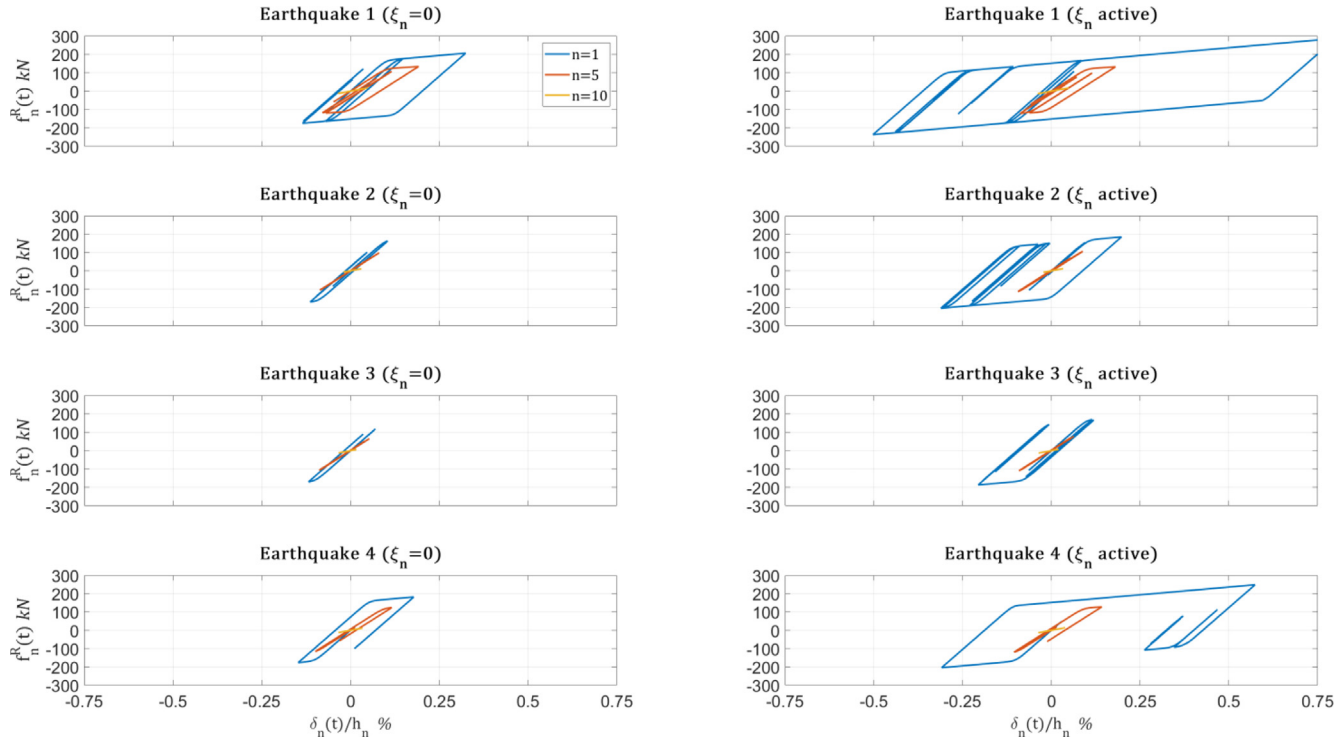

Fig. 7. Resisting shear force under no command voltage ($\xi_n = 0$) and active command voltage.

sampling time-step of 0.005s. Also, regarding the prediction model, the variance vectors are set as $\sigma^z = 0.021g/s$ and $\sigma^y = 0.021g/s$.

Fig. 5 depicts the elevation scheme of the addressed 10-story frame system. The story stiffnesses are calculated while assuming the columns of 4.0 m in length are clumped at both ends. The stiffness quantities relate to cross-sectional areas are of 30/100, 30/90, 30/80, and 30/60 in centimeters with a modulus of elasticity of $27 \cdot 10^6 KPa$. The stories' mass is set as 7.5ton which provides the following modal periods:

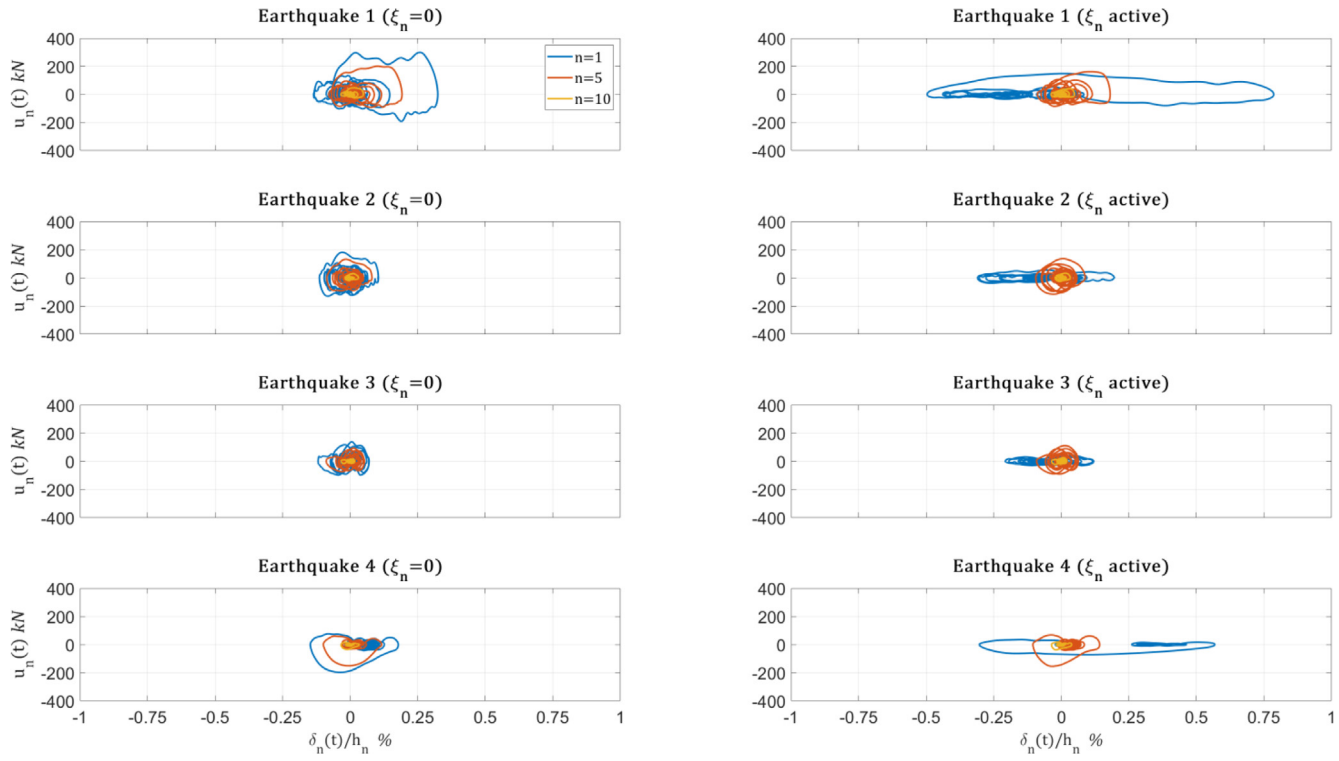

Fig. 8. SAFVD force under no command voltage ($\xi_n = 0$) and active command voltage.

Table 2
Maximum shear force (kN).

	No command voltage				Changing command voltage			
Story	**EQ. (1)**	**EQ. (2)**	**EQ. (3)**	**EQ. (4)**	**EQ. (1)**	**EQ. (2)**	**EQ. (3)**	**EQ. (4)**
10	52	34	24	38	36	32	26	35
9	100	67	48	75	73	64	52	69
8	163	80	68	102	109	92	73	99
7	196	106	90	135	145	115	91	123
6	242	139	109	153	181	138	104	149
5	267	164	129	181	216	160	124	175
4	293	184	146	203	250	182	144	200
3	335	218	166	215	283	202	165	225
2	364	238	181	237	315	220	185	252
1	395	253	194	254	340	240	206	275

$$T_v = \frac{2\pi}{\omega_v} = \begin{cases} v=1, \quad 1.0s \quad ; \quad v=6, \quad 0.079s \\ v=2, \quad 0.29s \quad ; \quad v=7, \quad 0.067s \\ v=3, \quad 0.16s \quad ; \quad v=8, \quad 0.059s \\ v=4, \quad 0.12s \quad ; \quad v=9, \quad 0.052s \\ v=5, \quad 0.10s \quad ; \quad v=10, \quad 0.045s \end{cases}$$

Fig. 6 simulates the change in damping ratio and command voltage under the four earthquake records regarding stories 1, 5, and 10. The four seismic simulations exemplify how the solution of the short horizon in 4 reduces the damping coefficient in the lower stories to reduce the shear forces. Figs. 7 and 8 compare the hysteretic resisting forces and SAFVD forces at the 1, 5, and 10 stories (i.e., f_1^R, f_5^R, f_{10}^R, u_1, u_5, u_{10})with and without changing command voltage. It is exemplified how the SAFVD force in the first story reduces. The overall maximum shear forces in each simulation and story are specified in Table 2.

Fig. 9 compares the total acceleration at stories 1, 5, and 10 under no command voltage and under the effects of inducing command voltage. Indeed, the reduction in acceleration response follows its correlation with the shear forces, according to Eq. (13). Table 3 specifies the maximum total acceleration with and without changing command voltage. Regarding the total acceleration, the performance of the prediction model developed in 5 is demonstrated in Fig. 10, which shows that the absolute error does not surpass half of the variance value. It might be worth noting that since the measurement noise is simulated using a random array, the plot in Fig. 10 is not a continuous line.

In essence, the SAFVD control strategy looks to reduce the damping coefficient optimally. Consequently, the energy dissipation capabilities of the frame system are deterred and the deformations increase. Fig. 11 exemplifies how the input energy increases when the control strategy takes effect due to the more significant interstory drifts. The maximum interstory drifts are given in Table 4.

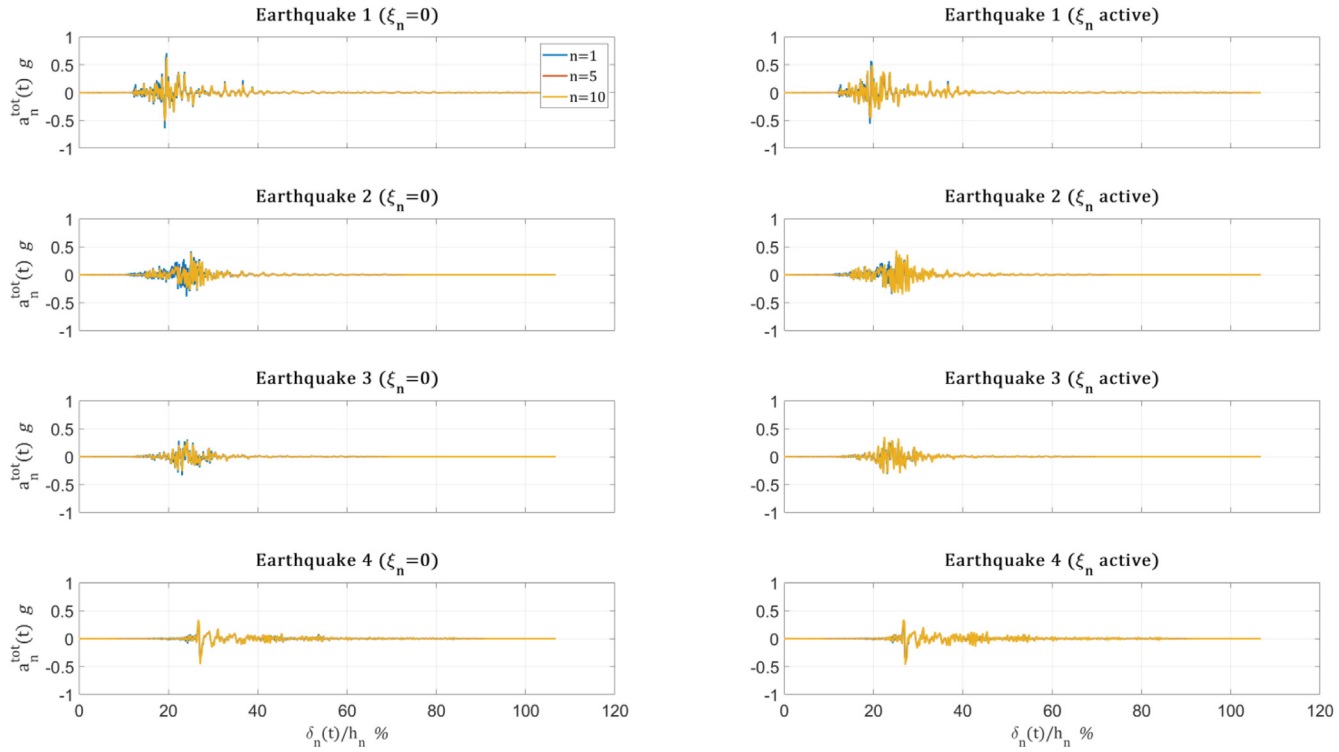

Fig. 9. Total acceleration under no command voltage ($\xi_n = 0$) and active command voltage.

Table 3
Maximum total acceleration (g').

	No command voltage				Changing command voltage			
Story	**EQ. (1)**	**EQ. (2)**	**EQ. (3)**	**EQ. (4)**	**EQ. (1)**	**EQ. (2)**	**EQ. (3)**	**EQ. (4)**
10	0.64	0.39	0.28	0.46	0.49	0.43	0.35	0.47
9	0.63	0.39	0.28	0.45	0.49	0.43	0.35	0.47
8	0.63	0.39	0.28	0.45	0.49	0.39	0.30	0.41
7	0.62	0.38	0.28	0.44	0.50	0.35	0.28	0.39
6	0.61	0.38	0.28	0.43	0.50	0.33	0.28	0.38
5	0.60	0.38	0.28	0.41	0.48	0.31	0.28	0.37
4	0.60	0.38	0.28	0.39	0.46	0.30	0.28	0.36
3	0.63	0.39	0.29	0.38	0.48	0.31	0.28	0.36
2	0.65	0.40	0.30	0.36	0.54	0.31	0.29	0.38
1	0.71	0.42	0.34	0.34	0.57	0.35	0.31	0.34

7. Conclusions

This paper develops a new strategy for controlling SAFVDs to reduce the shear forces applied to the columns of frame structures during seismic vibrations. The simulated closed-loop control feedback is the total acceleration measured by accelerometers placed on a chevron brace between columns. Since the acceleration readings correspond to the SAFVD plane, the development regards plane frame models. Still, the control law is also relevant to structures of irregular floor-plane (three-dimensional structures with torsional behavior). The concept of modifying and reducing the SAFVD damping coefficient is effective in lowering accelerations and applied shear forces. On the other hand, the interstory drifts slightly increase due to lower damping energy dissipation.

The proposed Kalman filter model predicts the sequential acceleration to cater to time delays and is modified to receive only the last two measurements to perform numerical integration. Hence, it does not require knowing the uncertainties regarding the frame structure (e.g., inelastic properties, inherent damping properties). While evaluating the subsequent time step's acceleration using more than two measurements may provide better accuracy, the proposed Kalman filter model corresponds to a state space formulation suitable for only the last two measurements. The case study shows that using the previous two measurements yields an error in the order of Δt^2.

The optimal change in command voltage is the solution to a short-horizon minimization problem. The objective function is the difference between the seismic inertia force and the SAFVD force, which equals the resisting forces produced by the columns. The Lagrange multiplier method yields the optimal conditions, leading to the optimal incremental time change in the SAFVD force. The relation between the change in SAFVD force and the change in command voltage is implicit. Thus, an alternative relationship is proposed based on the voltage change limit at each time step. The SAFVD effectiveness is exemplified by this paper's case study, which addresses a 10-story high-rise frame system. The case study demonstrates the efficacy of SAFVDs in reducing the maximum shear forces and total accelerations.

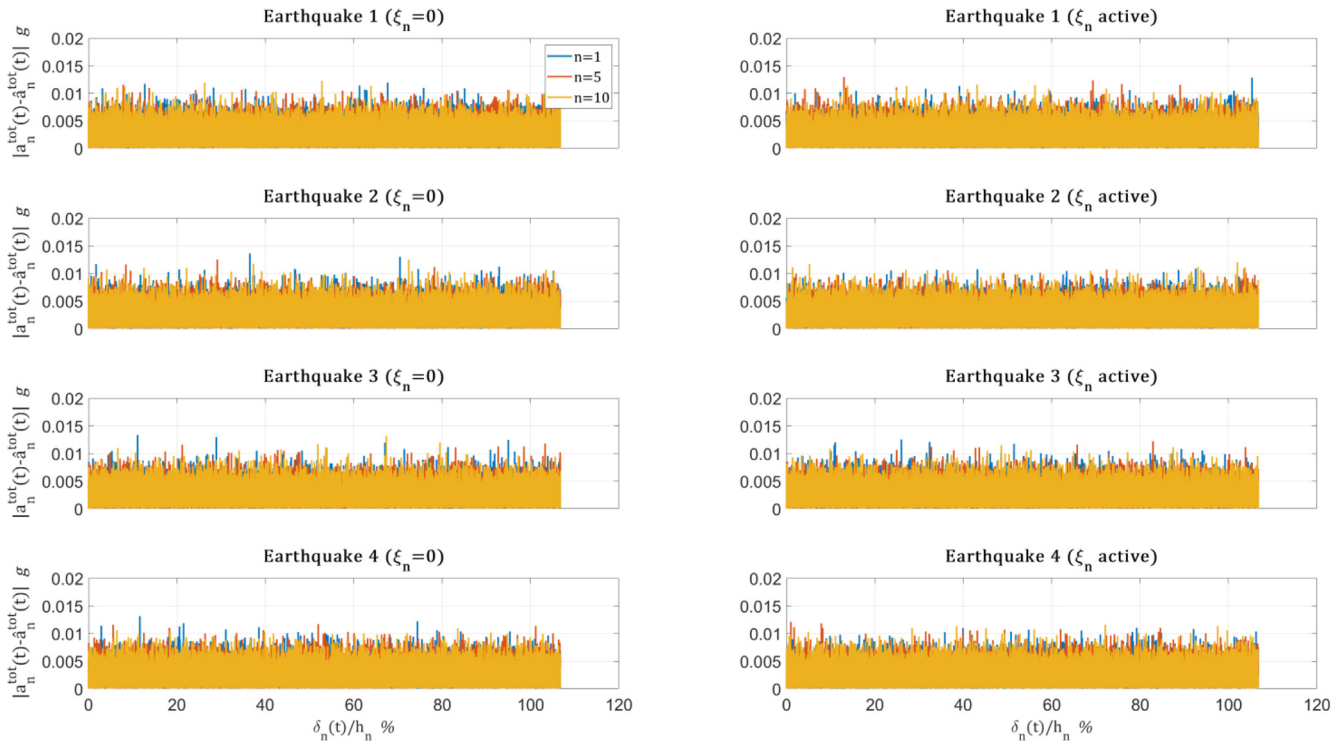

Fig. 10. The error of estimation of total acceleration using the prediction model.

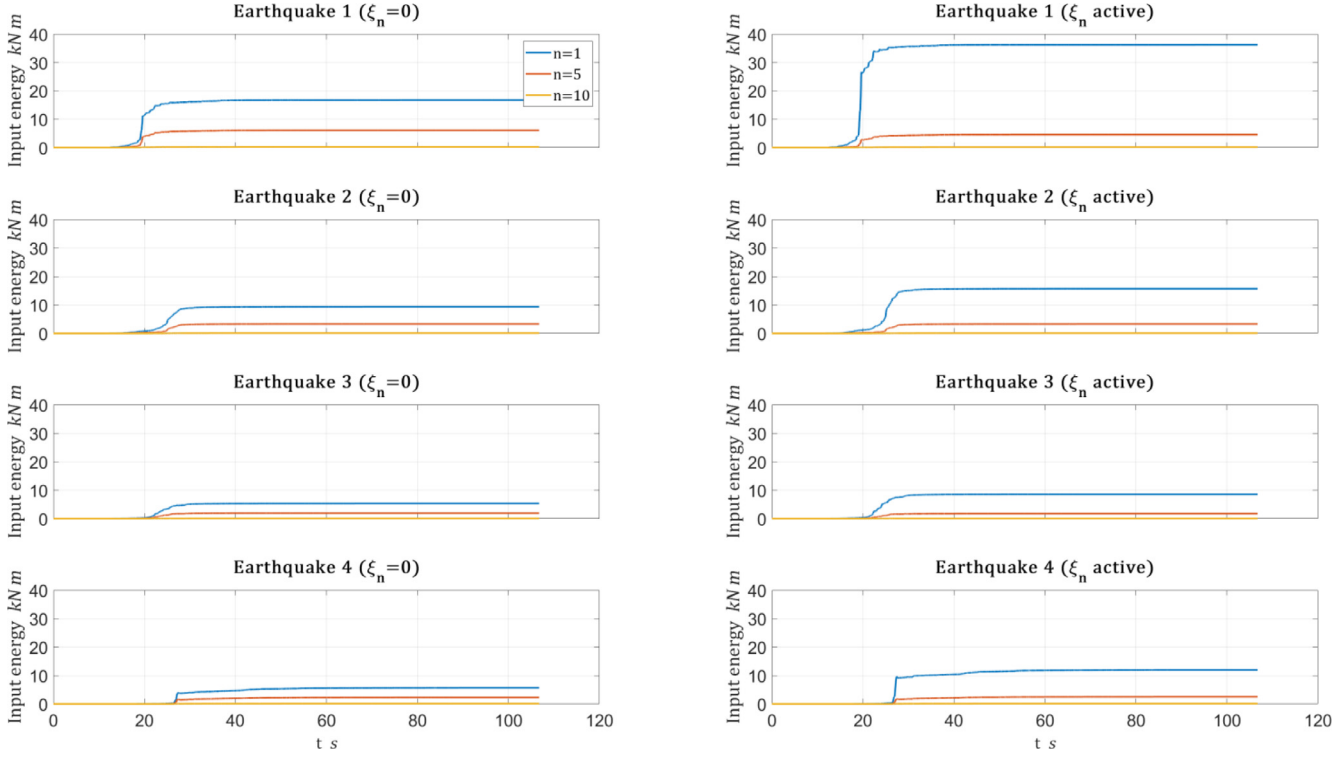

Fig. 11. Input energy under no command voltage ($\xi_n = 0$) and active command voltage.

Table 4
Maximum relative interstory drifts.

	No command voltage				Changing command voltage			
Story	**EQ. (1)**	**EQ. (2)**	**EQ. (3)**	**EQ. (4)**	**EQ. (1)**	**EQ. (2)**	**EQ. (3)**	**EQ. (4)**
10	0.20%	0.12%	0.13%	0.14%	0.19%	0.13%	0.14%	0.15%
9	0.39%	0.25%	0.27%	0.27%	1.32%	0.72%	0.51%	1.09%
8	0.39%	0.21%	0.23%	0.28%	0.60%	0.40%	0.30%	0.45%
7	0.57%	0.28%	0.31%	0.38%	1.46%	0.77%	0.40%	1.20%
6	0.56%	0.29%	0.29%	0.37%	0.53%	0.32%	0.30%	0.44%
5	0.77%	0.35%	0.35%	0.47%	0.72%	0.38%	0.37%	0.57%
4	0.99%	0.39%	0.42%	0.58%	0.94%	0.42%	0.44%	0.70%
3	0.88%	0.38%	0.36%	0.50%	0.82%	0.40%	0.37%	0.63%
2	1.09%	0.42%	0.41%	0.61%	2.62%	1.04%	0.56%	1.89%
1	1.30%	0.46%	0.47%	0.71%	3.14%	1.24%	0.82%	2.32%

Data availability

Data will be made available on request.

Declaration of Competing Interest

The authors declare that they have no known competing financial interests or personal relationships that could have appeared to influence the work reported in this paper.

References

[1] Soong TT, Constantinou MC. Passive and active structural vibration control in civil engineering, vol. 345. Springer; 2014.
[2] Chung LL, Lin RC, Soong TT, Reinhorn AM. Experimental Study of Active Control for MDOF Seismic Structures. J Eng Mech 1989;115:1609–27. https://doi.org/10.1061/(asce)0733-9399(1989)115:8(1609).
[3] Soong TT, Reinhorn AM, Wang YP, Lin RC. Full-Scale Implementation of Active Control. I: Design and Simulation. J Struct Eng 1991;117:3516–36. https://doi.org/10.1061/(asce)0733-9445(1991)117:11(3516).
[4] Reinhorn AM, Soong TT, Riley MA, Lin RC, Aizawa S, Higashino M. Full-Scale Implementation of Active Control. II: Installation and Performance. J Struct Eng 1993;119:1935–60. https://doi.org/10.1061/(asce)0733-9445(1993)119:6(1935).
[5] Spencer BF, Nagarajaiah S. State of the Art of Structural Control. J Struct Eng 2003;129:845–56. https://doi.org/10.1061/(asce)0733-9445(2003)129:7(845).
[6] Pall AS, Marsh C. Response of Friction Damped Braced Frames. ASCE J Struct Div 1982;108:1313–23. https://doi.org/10.1061/jsdeag.0005968.
[7] Pall AS, Pall R. Friction-dampers for seismic control of buildings–a Canadian experience. Elev world Conf Earthq Eng Acapulco, Mex 1996.
[8] Pasquin C, Leboeuf N, Pall T. Friction dampers for seismic rehabilitation of Eaton Building, Montreal. Proceedings, Annu. Conf. - Can. Soc. Civ. Eng., vol. 2002, 2002, p. 1771–80.
[9] McNamara RJ, Taylor DP. Fluid viscous dampers for high-rise buildings. Struct Des Tall Spec Build 2003;12:145–54. https://doi.org/10.1002/tal.218.
[10] Sabelli R, Mahin S, Chang C. Seismic demands on steel braced frame buildings with buckling-restrained braces. Eng Struct 2003;25:655–66. https://doi.org/10.1016/S0141-0296(02)00175-X.
[11] Taylor DP. Mega brace seismic dampers for the Torre Mayor project at Mexico City. 74th Shock Vib Symp 2003.
[12] Uang CM, Seible F, McDaniel C, Chou CC. Performance evaluation of shear links and orthotropic bridge deck panels for the new San Francisco-Oakland Bay Bridge. Earthq Eng Struct Dyn 2005;34:393–408. https://doi.org/10.1002/eqe.446.
[13] Xie Q. State of the art of buckling-restrained braces in Asia. J Constr Steel Res 2005;61:727–48. https://doi.org/10.1016/j.jcsr.2004.11.005.
[14] Tremblay R, Bolduc P, Neville R, DeVall R. Seismic testing and performance of buckling-restrained bracing systems. Can J Civ Eng 2006;33:183–98. https://doi.org/10.1139/l05-103.
[15] Yongqi C, Liangzhe M, Tiezhu C, Schneider R, Winters C. Shock control of Bridges in china Using Fluid Viscous Devices. Proc 14th World Conf Earthq Eng 2008:12–6.
[16] Di Sarno L, Manfredi G. Seismic retrofitting with buckling restrained braces: Application to an existing non-ductile RC framed building. Soil Dyn Earthq Eng 2010;30:1279–97. https://doi.org/10.1016/j.soildyn.2010.06.001.
[17] Dominguez A, Sedaghati R, Stiharu I. Modeling and application of MR dampers in semi-adaptive structures. Comput Struct 2008;86:407–15. https://doi.org/10.1016/j.compstruc.2007.02.010.
[18] Bahar A, Pozo F, Acho L, Rodellar J, Barbat A. Hierarchical semi-active control of base-isolated structures using a new inverse model of magnetorheological dampers. Comput Struct 2010;88:483–96.
[19] Mulay N, Shmerling A. Analytical approach for the design and optimal allocation of shape memory alloy dampers in three-dimensional nonlinear structures. Comput Struct 2021;249:. https://doi.org/10.1016/j.compstruc.2021.106518106518.
[20] Ikeda Y. Active and semi-active vibration control of buildings in Japan-practical applications and verification. Struct Control Heal Monit 2009;16:703–23. https://doi.org/10.1002/stc.315.
[21] Saaed TE, Nikolakopoulos G, Jonasson JE, Hedlund H. A state-of-the-art review of structural control systems. JVC/Journal Vib Control 2015;21:919–37. https://doi.org/10.1177/1077546313478294.
[22] Lu Z, Wang Z, Zhou Y, Lu X. Nonlinear dissipative devices in structural vibration control: A review. J Sound Vib 2018;423:18–49. https://doi.org/10.1016/j.jsv.2018.02.052.
[23] Shinozuka M, Constantinou M, Ghanem R. Passive and active fluid dampers in structural applications. US/China/Japan Work. Struct. Control 1992:507–16.
[24] Symans MD, Constantinou MC, Taylor DP, Garnjost KD. Semi-active fluid viscous dampers for seismic response control. Proceding 1st World Conf. Structrual Control. Univ. South. California, Los Angeles, vol. 3, 1994, p. FA4-3-FA4-l2.
[25] Symans MD, Constantinou MC. Seismic testing of a building structure with a semi-active fluid damper control system. Earthq Eng Struct Dyn 1997;26:759–77. https://doi.org/10.1002/(SICI)1096-9845(199707)26:7<759::AID-EQE675>3.0.CO;2-F.
[26] Seleemah AA, Constantinou MC. Investigation of Seismic Response of Buildings with Linear and Nonlinear Fluid Viscous Dampers. National Center for Earthquake Engineering Research Buffalo 1997.
[27] Zhang J, Agrawal AK. An innovative hardware emulated simple passive semi-active controller for vibration control of MR dampers. Smart Struct Syst 2015;15:831–46. https://doi.org/10.12989/sss.2015.15.3.831.
[28] Reigles DG, Symans MD. Supervisory fuzzy control of a base-isolated benchmark building utilizing a neuro-fuzzy model of controllable fluid viscous dampers. Struct Control Heal Monit 2006;13:724–47. https://doi.org/10.1002/stc.108.
[29] Waghmare MV, Madhekar SN, Matsagar VA. Semi-Active Fluid Viscous Dampers for Seismic Mitigation of RC Elevated Liquid Storage Tanks. Int J Struct Stab Dyn 2019;19:1950020. https://doi.org/10.1142/S0219455419500202.
[30] Bakhshinezhad S, Mohebbi M. Multi-objective optimal design of semi-active fluid viscous dampers for nonlinear structures using NSGA-II. Structures, vol. 24, Elsevier; 2020, p. 678–89. 10.1016/j.istruc.2020.02.004.
[31] Shi X, Guan X, Shen W, Xing L. A control strategy using negative stiffness and semi-active viscous damping for fully tracking active control force for bridge cables: Principles and simulations. Struct Control Heal Monit 2022;29:. https://doi.org/10.1002/stc.2989e2989.
[32] Xu Z, Agrawal AK, Yang JN. Semi-active and passive control of the phase I linear base-isolated benchmark building model. Struct Control Heal Monit 2006;13:626–48. https://doi.org/10.1002/stc.102.
[33] Ying ZG, Zhu WQ. A stochastic optimal time-delay control for nonlinear structural systems. Struct Eng Mech 2009;31:621–4. https://doi.org/10.12989/sem.2009.31.5.621.
[34] Duc-Chuan V, Ioannis P, Sette D. A new algorithm for semi-active control of mixed base isolation. Procedia Eng 2017;199:1785–90. https://doi.org/10.1016/j.proeng.2017.09.457.